Experimental and Numerical Performance Evaluation of a Modified sCO2 Compressor Blade Profile to Reduce Leading Edge Condensation

Erik Fernandez
Research Associate Professor
University of Central Florida, Center for Advanced Turbomachinery and Energy Research (CATER)
Orlando, FL. USA

Emmanuel Gabriel-Ohanu
Graduate Research Assistant
University of Central Florida, Center for Advanced Turbomachinery and Energy Research (CATER)
Orlando, FL. USA

Ladislav Vesely
Research Assistant Professor
University of Central Florida, Center for Advanced Turbomachinery and Energy Research (CATER)
Orlando, FL. USA

Jayanta Kapat
Professor
University of Central Florida, Center for Advanced Turbomachinery and Energy Research (CATER)
Orlando, FL. USA

Ashvin Hosangadi
Vice President CRAFT Tech
Combustion Research and Flow Technology (CRAFT Tech)
Pipersville, PA. USA

Tim Weathers
Research Scientist
Combustion Research and Flow Technology (CRAFT Tech)
Pipersville, PA. USA

Antonio Cepero
Assistant Research Scientist
Combustion Research and Flow Technology (CRAFT Tech)
Pipersville, PA. USA

Paul Cooper
Consultant to CRAFT Tech
Combustion Research and Flow Technology (CRAFT Tech)
Pipersville, PA. USA

Presenter Bios: Erik Fernandez is a Research Assistant Professor at the University of Central Florida, and a project manager for the Center for Advanced Turbo Machinery and Energy Research. His research has focused on Active Flow Control, Turbomachinery fluid mechanics and heat transfer, laser-based optical flow diagnostics, Experimental methods for Supercritical Carbon Dioxide, and Adsorption-Based Hydrogen Storage Systems.

Ashvin Hosangadi is a Vice-president and founding member of CRAFT Tech. He leads the development team at CRAFT Tech for the CRUNCH CFD® code. Dr. Hosangadi has extensive experience in modelling turbomachinery with phase change for real fluids and has simulated full-scale sCO2 compressors for CSP applications.

ABSTRACT

The primary compressor is one of the key components in a supercritical carbon dioxide (sCO$_2$) power cycle; it operates with inlet conditions just above the critical point of CO$_2$ to maintain high fluid density and reduce power requirements. However, with rapid variations of properties near the critical point, and its proximity to the saturation dome, it makes the compressor susceptible to multi-phase effects. Local flow acceleration at the leading-edge of compressor blades can lower local static temperature and pressure, leading to the local thermodynamic state dropping into the saturation dome. With sufficient subcooling, condensation nuclei are initiated, leading to the formation, and growth of liquid droplets Multi-phase effects can lead to loss of compressor efficiency, and potentially damage turbomachinery components.

A numerical study has been performed to evaluate the performance of a novel compressor leading-edge/suction side design; it is benchmarked against a typical, constant thickness, compressor blade. This study explores the improved blade performance in a 3-pass linear cascade which is consistent with that of the concurrent experimental study. Performance metrics evaluated include velocity, pressure, and temperature fields, associated blade temperature surface distributions, and condensate concentration fields (liquid mass fraction). A range of inlet conditions are run to evaluate the sensitivity of the improved blade design to coincide with cascade relative velocities which cover a range of moderate to high flow coefficients for a typical centrifugal compressor; these include cases covering the range of operation of the Hanwha/GE compressor used in the Sunshot program. The improved Biased-Wedge design is shown to mitigate multi-phase effects at these relevant flow conditions, including those of the Hanwha/GE compressor for compressor inlet temperatures of 310K. To support the numerical work run by CRAFT Tech, an experimental effort is conducted to validate numerical results, in a 3-pass linear cascade. These experiments will be run in a first of its kind sCO$_2$ optical diagnostics rig, which allows for the visualization, and velocimetry measurement of supercritical flows using advanced laser-based diagnostics. The novel test section, implementation of optical diagnostics, challenges, and integration into the UCF sCO$_2$ flow and heat transfer loop will be discussed in detail.

INTRODUCTION

The main compressor is one of the key components in a supercritical carbon dioxide (sCO$_2$) power cycle; it operates with inlet conditions just above the critical point of CO$_2$ (31°C and 73.8 bar) to maintain high fluid density and reduce power requirements. An innovative approach is developed to mitigate multi-phase effects at the leading-edge region of compressor impeller blades for supercritical carbon-dioxide flow near, but above the critical point. Rapid variations of properties near the critical point and its proximity to the saturation dome makes the compressor susceptible to multi-phase effects.

Figure 1 illustrates that local flow acceleration at the leading edge on the suction surface results in lower local static temperature and pressure, causing the thermodynamic state to potentially drop into the saturation dome. With sufficient subcooling, condensation nuclei are initiated, leading to growth of liquid droplets. Although these droplets may not immediately impact the compressor's performance, their high relative velocities can cause material erosion at the leading edge, thereby reducing the compressor's lifespan and efficiency in the long run as the blade surface undergoes modifications.

Currently, condensation is avoided by compressor designers through the requirement of inlet conditions having a larger margin above the critical point. However, this is undesirable
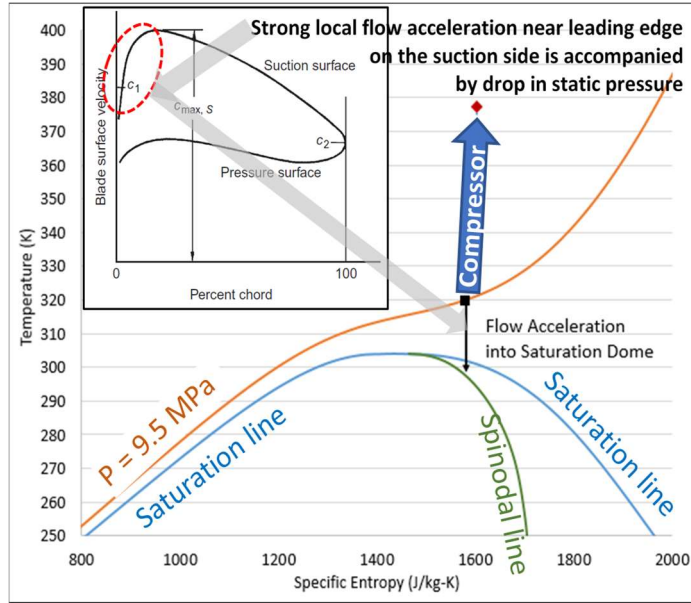
Figure 1: T-s diagram: local flow acceleration [1] (inset: local velocity outside boundary layer around the surface of a compressor airfoil, from ref.) [2]

because it leads to a drop in fluid density, subsequently increasing the compressor's power requirement. In this study, ***a novel design methodology for the leading-edge suction surface is proposed to substantially reduce pressure and temperature drop***, thereby minimizing the likelihood of condensation under design conditions. Moreover, this innovative design methodology does not adversely affect compressor performance and can be retrofitted into existing designs. Adapted from its original application in high-energy centrifugal pumps, where it significantly reduced cavitation and associated erosive damage, this design methodology deviates from conventional pumps and compressors with blades of nearly constant thickness. These blades may be tapered to a smaller rounded nose at the leading edge. Analysis of the pressure distribution on such blades reveals a significant drop or spike on the suction side to pressures well below the vapor pressure, as depicted in Figure 2 (from [3]). By expanding the
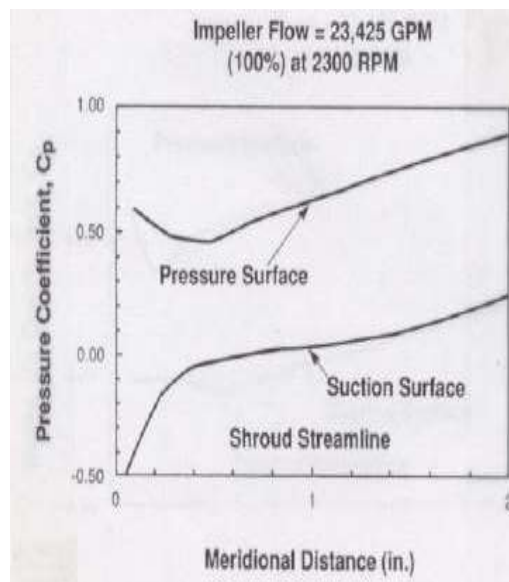

Figure 2: Pressure Distribution on a Conventional Impeller Blade

suction side of the impeller blade to resemble more of an airfoil, a "Biased-Wedge" is created. This new suction side blade shape, along with other advantageous features, is illustrated in Figure 3 (from [4]). The design's advantage lies in the resulting camber aligning the leading edge better with the incoming relative flow, thus avoiding the substantial incidence of a conventional blade. The resulting pressure profile on the suction surface of the blade is shown in Figure 4. As evident, there is negligible pressure drop on the suction surface for the "biased wedge" blade leading edge. Field experience in full-scale, high-energy pumps has shown a virtual elimination of cavitation damage using this approach [5]. It is believed that similar improvements can be anticipated with near-critical CO_2 by significantly reducing phase change and extending the range of compressors on the high-flow coefficient side of the curve.
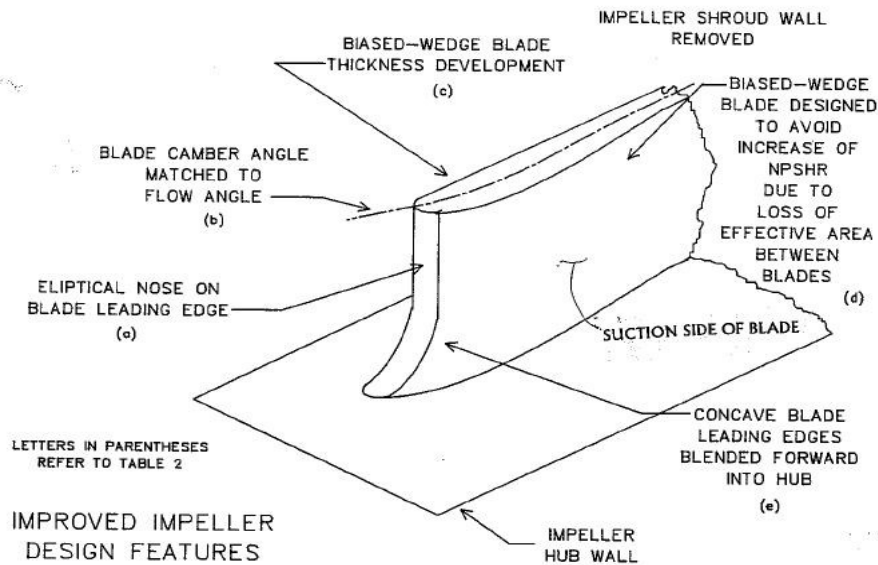

Figure 3: Biased-Wedge Impeller Blade to Reduce Pressure Drop on Suction Surface
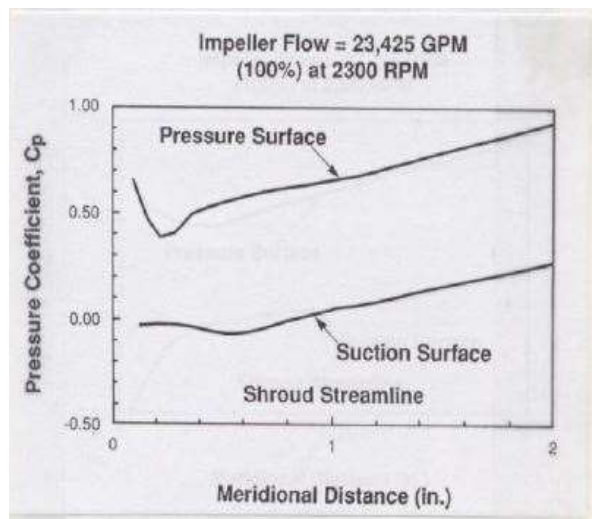

Figure 4: Pressure Distribution on a Biased-Wedge Impeller Blade

sCO₂ Performance Sensitivity to Inlet Temperature

- Two Key Issues:

  1. Peak efficiency values drop substantially as inlet temperature comes closer to critical temperature and the entire efficiency curve is lower as can be seen in in the isentropic efficiency vs flow coefficient plot of Figure 5 [6].

  2. Drop-off at the higher flow rates is steeper; this substantially reduces the range of the compressor at lower inlet temperatures. These drop offs occur at lower and lower flow coefficients as the inlet temperature is incrementally reduced towards the critical temperature. These subcritical effects can further be visualized by the liquid mass fraction iso surfaces in Figure 6. As the compressor flow coefficient increases, larger regions of liquid condensate form at the leading edges and shroud. These are coupled to the temperature fields, and as shown, the local temperatures get subcritical in the lower figures of Figure 6 [6]. The regions of highest flow acceleration are at the compressor leading edges, and are outlined by these subcritical temperature regions.
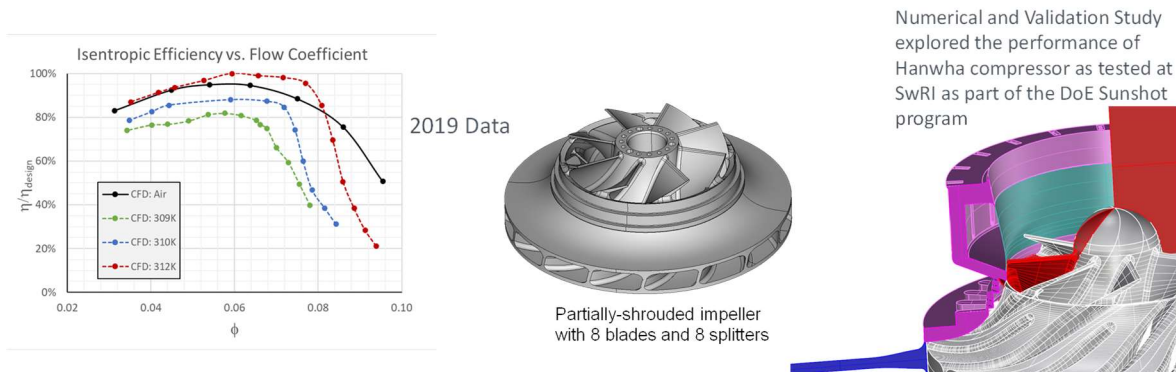

Figure 5: sCO₂ Performance Sensitivity to Inlet Temperature [6].

- ***Cause for #1 potentially associated with leading blade design that disrupts flow into the splitter blade at lower inlet temperatures causing blockage and mixing losses***

- Cause for #2 is associated with phase change in the inlet "throat" leading to blockage

In this investigation, CRAFT Tech supported the development of a cascade test loop (UCF) featuring both conventional and biased wedge blades. These blades simulate the flow around the leading-edge of a rotating compressor blade, enabling the assessment of the impact of leading-edge design on suction side condensation under various sCO₂ conditions. As these experiments are conducted within a stationary test loop (i.e. non-rotating), the flow around the blade is simulated in the relative frame of reference (from a compressor perspective.) CRAFT Tech, with guidance from consultant Dr. Paul Cooper, undertook the design of the cascade and the test section, while the UCF team executed the transition of the cascade design to a physical testing apparatus. The cascade test section was designed and integrated into a sCO₂ optical diagnostics pressure vessel plumbed into UCF's flow and heat transfer loop.

First of their kind quantitative flow measurements using Particle Image Velocimetry (PIV)
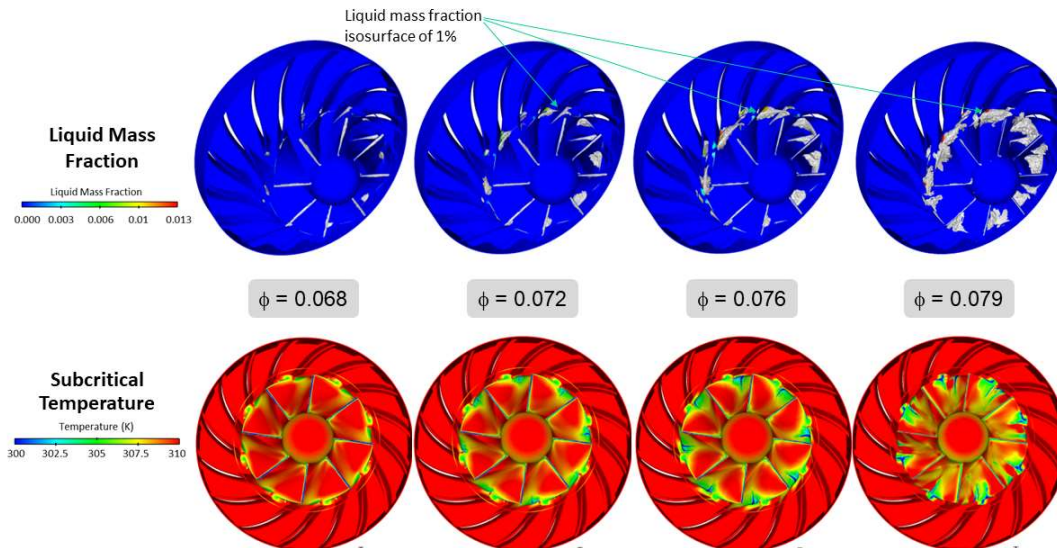
Figure 6: Subcritical Effects at Shroud Inlet at High Flow Rates [6].

were performed on the two blade geometries of interest. These results were used to evaluate the Biased-Wedge performance, and to validate subsequent numerical results. Simulations were conducted at both the flow conditions available at UCF for CFD validation, as well as higher flow rates at conditions more realistic of higher energy compressor configurations. These simulations were conducted with the CRUNCH CFD® code [6] developed at CRAFT Tech. The CRUNCH CFD® code has an advanced real fluid formulation with both equilibrium and non-equilibrium phase change and droplet condensation options and has been used to model sCO$_2$ compressors with phase change such as the Sandia compressor and Hanwha's compander under the DoE Sunshot program. The objective of the study is to demonstrate that the Biased-Wedge design can be a viable design option to reduce phase change, improve performance, and extend the range of sCO$_2$ main compressors.

Methodology

CRUNCH CFD® Overview

The numerical framework of the CRUNCH CFD® software features an advanced preconditioning framework for real fluid systems [7], [8]. One of the key attributes of this numerical formulation is that it alleviates the numerical stiffness resulting from strong thermodynamic property variations both near the critical point, as well as at subcritical conditions where phase change can result in sharp variations in acoustic speed and density. Specifically, it allows for sharp variations in the derivatives of density and enthalpy near the critical point to be modeled faithfully, leading to improved results with more robustness near the critical point.

The numerical formulation requires the specification of density, enthalpy, and their derivatives ρ_P, ρ_T, h_P, h_T as a function of local pressure and temperature. As an alternative to analytical equation of state models, a table look-up procedure generated from the NIST database [9] has been implemented to obtain thermodynamic properties, their derivatives, as well as transport properties i.e., viscosity μ, and thermal conductivity k, as a function of input pressure and temperature using bilinear interpolation. Extensions of the table look-up procedure for subcritical conditions, where liquid and vapor properties must be evaluated independently, are described in Hosangadi et al. [10].

Phase change is modeled within a "two-fluid" framework (see Ref [10 for details) wherein separate mass conservation transport equations for liquid and vapor are solved. However, the two components are assumed to have the same local conditions and hence, only mixture conservation equations for momentum and energy are solved. Phase change is driven by local conditions; a finite rate phase change model that is based on the difference between the fluid pressure relative to the saturation pressure at the local temperature is implemented. In Equation 1 below, the net mass transfer is given by m_t and is comprised of vaporization and condensation terms that drive the solution to pressure equilibrium:

$$m_t = K_f \rho_L \phi_L + K_b \rho_g \phi_g$$

$$K_x = \begin{bmatrix} 0 & p < p_v \\ \dfrac{1}{\tau_x^*} & [\dfrac{p - p_v}{\dfrac{1}{2}\rho_\infty V_\infty^2}] & p > p_v \end{bmatrix}$$

(1)

where τ_f^* is the non-dimensional time scale for vapor formation in seconds and τ_b^* is the non-dimensional time scale for liquid condensation in seconds.

Validation for the Sandia compressor over a broad range of conditions spanning the saturation dome with significant multi-phase effects has also been performed. Details of these validation studies are presented in Hosangadi et al. [10] and Brinckman et al. [11] A rigorous evaluation for the 10 MWe Hanwha Apollo has been conducted over a wide range of flow coefficients and inlet temperatures and presented in Hosangadi et al. [6]. Comparison of pre-test predictions with test data acquired showed good match and accurate predictions of performance trends as shown in Figure 7. Flow coefficient, head coefficient, and efficiency are defined below, in (2). Here, Q is the flow rate, r is the impeller exit radius, U is the tip speed at the impeller exit radius, and H is total enthalpy. Subscript 1 corresponds to the compressor inlet, subscript 2 to the volute exit, and i corresponds to isentropic.

$$\phi = \frac{Q_1}{\pi r^2 U} \qquad \psi = \frac{2(H_{2i} - H_1)}{U^2} \qquad \eta_i = \frac{(H_{2i} - H_1)}{(H_2 - H_1)} \qquad (2)$$
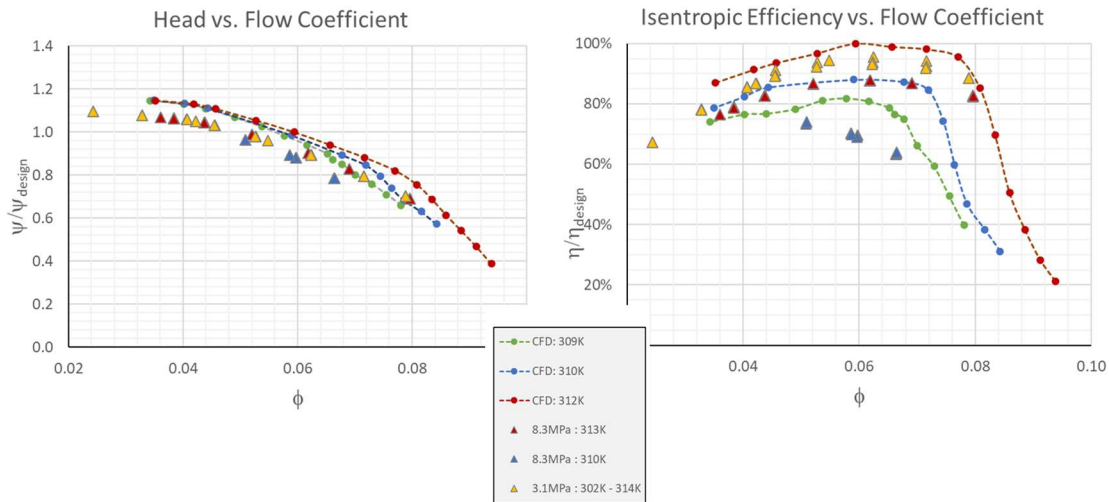

Figure 7: Performance Comparisons for Hanwha 10 Mwe Compressor [6]

Cascade Design for sCO$_2$ Testing

The cascade design and test section geometry has been tailored to the flow rate that can be provided by the pump at UCF. The details of the design are provided in the following sub-sections below: a) inlet conditions, b) cascade parameters, c) blade shape details.

Inlet Conditions

The maximum volumetric flow rate of the pump in the UCF loop is 16.5 liters/min. For the design calculations here, we have assumed a volumetric flow rate of 14.5 liters/min. The nominal sCO$_2$ inlet conditions are assumed to be 85 bar and 310 K. At these conditions the density is 514.87 kg/m3 and viscosity: 36.995 µPa-s. The inlet pipe has a 1" OD and 0.760" ID and the pipe velocity based on ID is 0.8257 m/s (2.708 ft/s). The pipe Reynolds number is 221,831 which is fully turbulent.

Cascade Parameters

The cascade section has been designed to simulate a centrifugal compressor inlet with a flow coefficient of 0.49 which corresponds to an inlet flow angle of 26° (with the vertical). The blade height in the cascade is set at 10 mm. Preserving cross sectional area corresponding to the inlet pipe flow area, yields the width of cascade *normal to flow direction* as 29.267 mm. Therefore, width of cascade along axis (i.e. vertical) direction is 66.76 mm (=29.267/sin(26)). We assume a solidity of 2.6 which is typical for centrifugal compressors and design for zero incidence at the leading edge. Therefore, the blade angle is also 26°.

The cascade is designed for two blades or 3 passages in cascade. Therefore, spacing S is 22.25 mm (=66.76/3). The chord length is computed from spacing and solidity as 57.86 mm (=22.25 x 2.6). The length of blade along axis in Z is 25.36 mm (C x sin(26)). For simplicity of the manufactured cascade rig, the decision was made to keep a constant blade span for the test section, with a thickness of 10 mm.

Blade Shape

A schematic of the biased wedge blade is shown in Figure 8. The pressure side of the blade is flat while the suction surface features the biased wedge design for condensation/phase change control. The full thickness of the blade at the trailing edge is 1.5 mm. The throat of the cascade passage is at a length of 20 mm. The biased wedge on the suction surface extends beyond the throat to 25.94 mm. The maximum thickness of the biased wedge is estimated to be 3.00 mm (or 2 times the trailing edge thickness) and the maximum thickness occurs at a distance of 12.54 mm
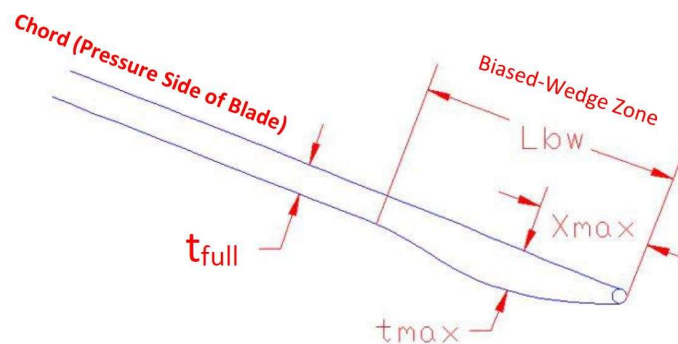

Figure 7: Schematic of Blade Shape Illustrating Biased Wedge

(or 0.6269 chord length). The nose of the leading edge will have a 2:1 elliptical shape.

Cascade Layout

The three-pass cascade was designed for interchangeability between the Baseline constant thickness blade, and the Biased-Wedge. Due to the limited number of passes, the upper and lower wall treatments were crucial to ensure adequate periodicity across the blades, particularly the lower blade, which would be the one to be evaluated experimentally. Various wall treatments and tailboard angles were evaluated numerically. The best performing treatment was a simple, flat upper, and lower wall, as shown in the flow fields in Figure 9. This also helped in the transition to experiment, as flat upper and lower walls would be simpler to implement, as well as maintaining better optical clarity for the laser sheet which would need to pass through the top and bottom walls.
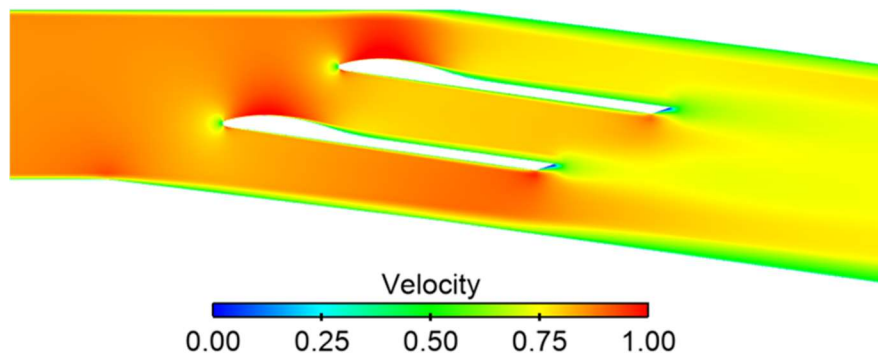
Figure 8: Contour plot of velocity (m/s) from 3D simulation of Configuration 3

Experimental Setup

To experimentally assess the performance of the Biased-wedge blade profile to validate the companion numerical results, the fluid domain designed by the CRAFT group was transitioned to an experimental apparatus to be integrated into UCF's supercritical CO_2 flow and heat transfer loop. Due to the challenges of the high-pressure sCO_2 environment, conventional experimental methods oftentimes easily implemented with air, had to be thoroughly addressed to achieve viable, and accurate results for blade performance assessments. Rig design, test section integration, manufacturing tolerance assessment, and experimental challenges, and application of quantitative optical diagnostics will be discussed herein.

Figure 10 shows the flow loops at UCF, and summarizes their capabilities. In this study, the High Temperature/Pressure rig's high flow recirculation pump (Sigma Pumpy Hranice Ltd.), was used in conjunction with the Near Critical point rig; this leveraged the advantages of the high flow rate, and the simplicity of the smaller loop.
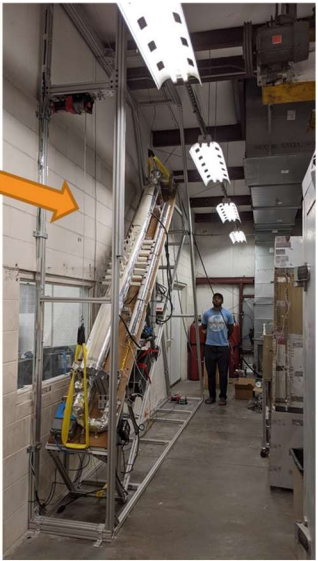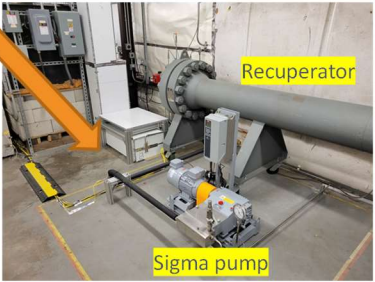
Figure 10: UCF sCO₂ Loop Selection for Experimental Effort

With the need for optical diagnostics, a previously built pressure vessel was used to house the manufactured linear compressor blade cascade. Details of the optical diagnostics rig, and linear cascade will be discussed in subsequent sections. The loop schematic as tested, and the optical diagnostics vessel are shown in Figure 11. In the testing configuration for this study, the non-recuperated loop is driven by the large recirculation pump borrowed from the other loop (shown as "gear pump" in Figure 11). Flow travels through the Coriolis mass flow meter, and through several preheating sections before entering the optical diagnostics test section. Flow then exits the test section, is cooled by a water chiller system, and re-enters the recirculation pump. Flow conditions are measured via a Rheonik Coriolis mass flow meter, several absolute pressure transducers located at the test section inlet and pump inlets, fluid bulk temperature thermocouple probes, and fluid bulk temperature high-accuracy Platinum Resistance Temperature Detectors
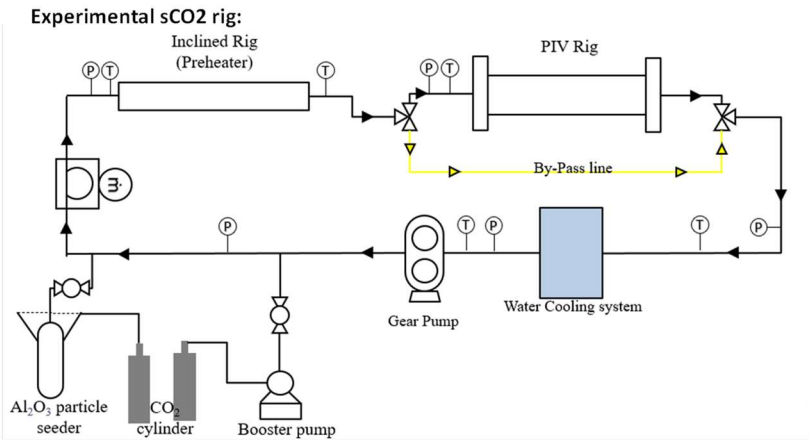
- Non-Recuperated
- Operating Pressure: 70 – 100 Bar
- Operating Temperatures: 20C – 100C (293K – 373K) (Optical Diagnostics Test Section Vessel Limitation)
- Mass flow rates up to 3.6 kg/min @90Bar

The operating pump was changed from the gear pump to the sigma pump (piston type) due to higher flow rate capability

Figure 11: sCO₂ Loop for cascade testing

(RTDs). Due to the proximity of these testing conditions to the CO_2 critical point, temperature measurement accuracy is paramount to keeping measurement uncertainties manageable.

Experimental Cascade Test Section

Based on the resultant linear cascade geometry provided by CRAFT, the UCF experimental group's next task was to transition this fluid domain geometry into a physical linear cascade that could be integrated into the sCO_2 loop to be used, in conjunction with the optical test section pressure vessel. Since the vessel would be taking the pressure force, the linear cascade test section could be manufactured from thin stock, and more easily manufacturable materials such as PVC and aluminum, and thin quartz glass. A modular test section was designed which consisted of two main walls, and thin upper and lower walls. The assembled section is shown in Figure 12; note the walls are held in place via dowel guide pins and thru-bolts to clamp the test section together. This configuration was chosen since the test section would have to be disassembled several times to change the blade configuration, and to clean out deposited solid particles left over from PIV tracer particle seeding. Note also on the cascade trailing edge, adjustable tailboards were installed. While the inlet flow and geometry should behave close to ideal, as in the simulations, the tailboards will allow for fine tuning of the flow in case the leading-edge stagnation point is biased to the suction side. In the final configuration, it was noted that the flow indeed had a slight suction side bias, and the tailboards were adjusted to an exit angle of 7˚, compared to the initial 8˚ configuration.

The cascade test section is instrumented and assembled using nuts and bolts to maintain its structural integrity for the proposed experiments.
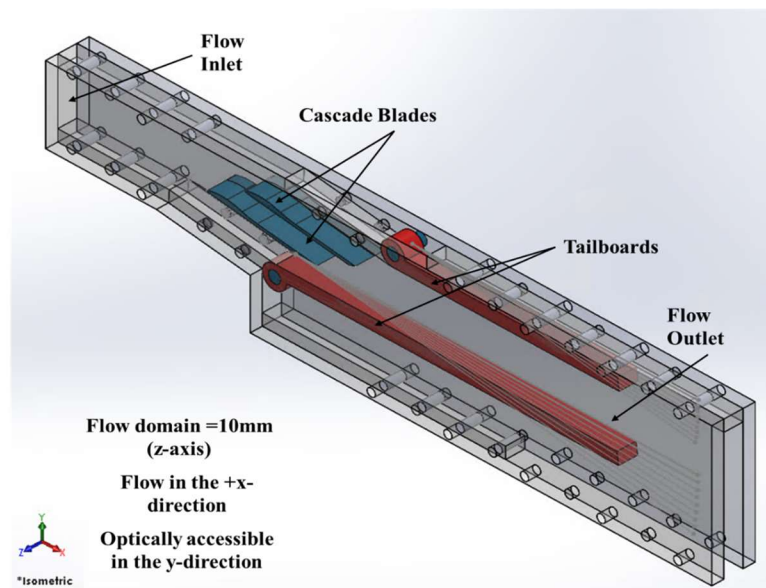

Figure 12: Assembly and Sections of Cascade Test Section

Cascade Test Section as Manufactured and Integrated

The initial iteration of hardware was manufactured out of clear PVC due to ease of manufacture and optical clarity, the test section completed assembly is shown in Figure 13. Guide dowels, and bolts are used to assemble the test section. Upper, lower and side walls are manufactured from un-machined acrylic to ensure optical clarity. The back wall for this configuration was scribed with angle marks for tailboard angle measurement. Note, in the final test section iteration, aluminum was used instead of PVC for the front and back walls; this will be discussed in subsequent sections.
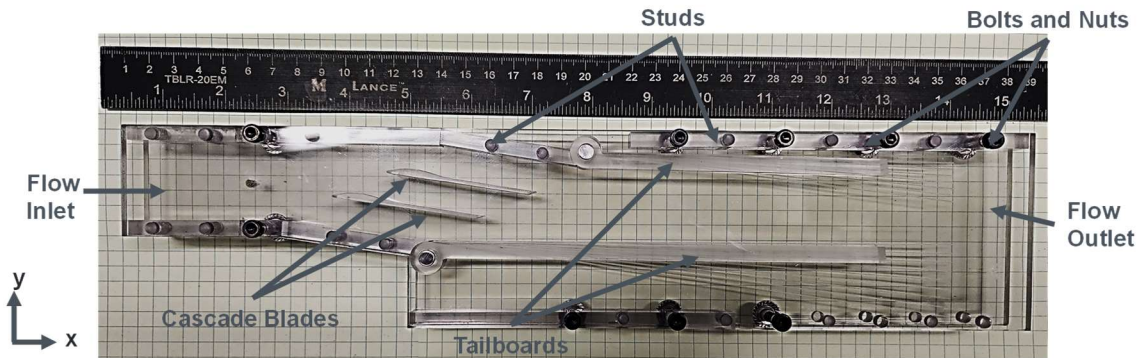

Figure 13: Cascade Test Section as manufactured (First Iteration)

While the sCO$_2$ loop is instrumented throughout for pressure and bulk flow temperature measurement, additional calibrated thermocouples were installed just upstream of the cascade section to serve as redundant measurements to support the RTD bulk flow measurements upstream. The TC beads protrude 1mm into the flow on the side, upper, and lower upstream walls, and are 28.1mm upstream of the cascade start.

The 3d printed transition nozzle connector is shown in Figure 14 attached to the cascade inlet. 3d print brass anchors are embedded into the transition nozzle to aid in the assembly clamping. Stainless-steel set screws and guide bolts clamp the sections and the upstream pipe together.
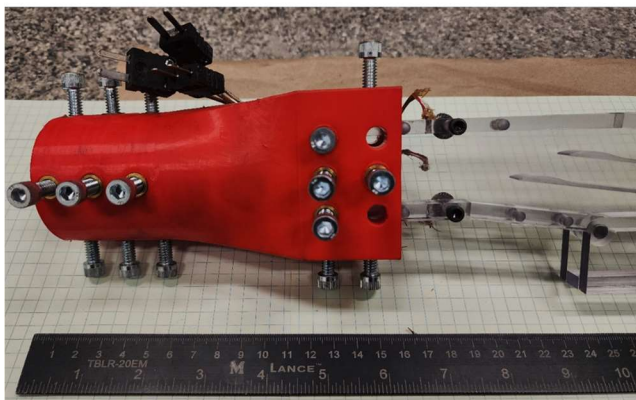
- 3D printed ABS transition piece to connect the circular tube to cascade test section inlet
- The nozzle connector is instrumented with heat inserts and screws in order to tighten/secure the connection of the inlet tube and the test section
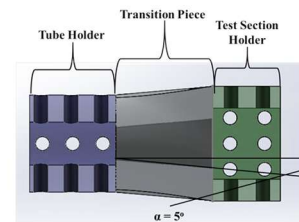
Figure 14: Cascade Test Section with Nozzle Connector

The complete rig assembly before pressure vessel integration is shown in Figure 15. The 1" diameter stainless steel pipe comes from the sCO_2 loop and enters the pressure vessel via a Swage-Lok thru fitting which is attached to the 6" ANSI flange with NPT threads. The nozzle transition and test section, then attach to the stainless-steel pipe within the pressurized vessel. Internal vessel temperature information is transferred out of the pressurized domain via Conax NPT thermocouple gland fittings. These glands bolt into NPT threads on the 6" blind flange. Due
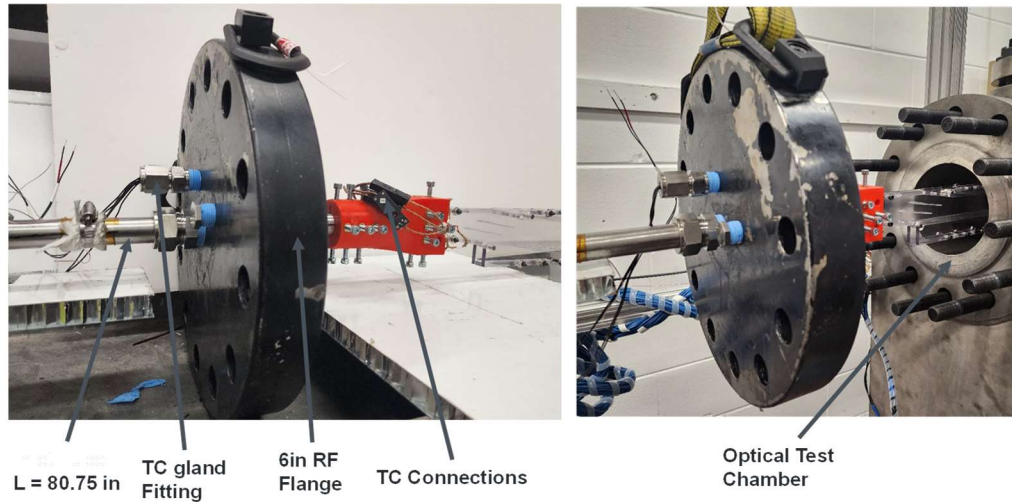

Figure 15: Experiment Assembly for Optical Test Chamber

to the weight and size of the flange and test section assembly, the entire flange is supported through an overhead hoist to aid in assembly and disassembly.

Experimental Challenges

The extreme variation in density, and resultant refractive index, pose large issues in any optical based diagnostic in supercritical fluids near their respective critical points. This density variation in the range of the proposed experiments is shown in Figure 16. Efforts were made to keep the internal pressure vessel temperature adequately isothermal by using segmented heaters with individual control. While this methodology was capable of maintaining the vessel temperature within 1°C at the measurement domain, this variation at the tested bulk inlet temperatures correspond to a density variation between 10-15%. While this variation is not massive, when one considers the total line-of-sight distance from the exterior optical window to the illuminated laser plane at the center of the test section is 8.25",this is enough to completely blur out any tracer particle images. A solution to "cut through" the density variations of the sCO_2 was needed. To do this, an optical light guide in the form of a solid optical quality cylinder, was placed in the line-of-sight between the exterior optical window and the clear cascade wall; in this configuration, the only density gradient to be imaged was across half of the cascade fluid domain (5mm) which was at a uniform temperature. Figure 17 shows the light guide rod concept integrated into the vessel. The first phase of this trail used a cast acrylic rod as the light guide. This worked well for the first few minutes of high-pressure operation, however eventually due to the amorphous nature of clear plastics, CO_2 started to adsorb into the plastic, cause crazing to occur on the surfaces, thereby degrading the optical quality. The setup next transitioned to a 50mm OD quartz rod which was

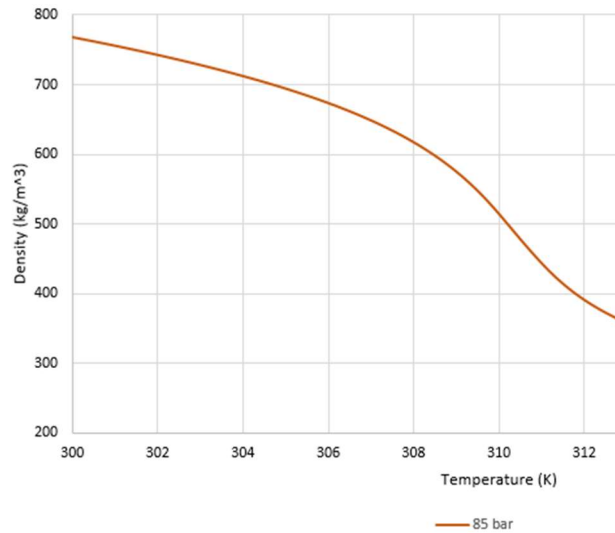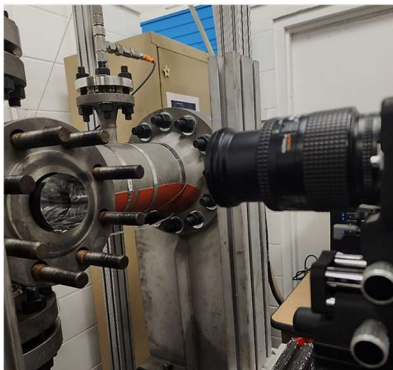immune to these issues, and was used for the final testing configuration.

Figure 16: CO_2 Density vs. Temperature in the range of the experiment

Figure 17: Optical light guide installed in pressure vessel

Particle Image Velocimetry (PIV) – Motivation and Background

Given sCO_2's need for pressure containment for its applications, fluid mechanics and heat transfer diagnostics are severely limited, particularly for techniques which can provide high spatial resolution velocity or temperature fields. An added challenge for this linear cascade performance evaluation, is scale. With a leading edge and blade thickness of 1.5mm, surface pressure taps would be nearly impossible at the required spatial resolution, and further complicated with the high-pressure environment and piping to exterior pressure transducers. To meet the requirements of this project, a non-intrusive, high spatial resolution, optical based technique will be required. The ideal candidate is Particle Image Velocimetry. PIV is a laser-based optical flow diagnostic in

which a two-dimensional plane is illuminated by a dual-pulsed laser with appropriate optics. Appropriately sized tracer particles are injected into the fluid domain or loop, and through Mie Scattering, are imaged by the laser plane. A high-speed camera synchronized to the laser pulses, images the tracer fields. A schematic of the PIV concept and the PIV setup used in this study, are shown in Figure 18. The two laser pulses are separated by a short time duration, generally on the order of microseconds. These two image pairs are then cross-correlated to estimate displacement vectors for the tracer field. With knowledge of the pixel to physical length scale, a velocity estimate can be made. The reader is referred to reference [12], for full details of the PIV technique.
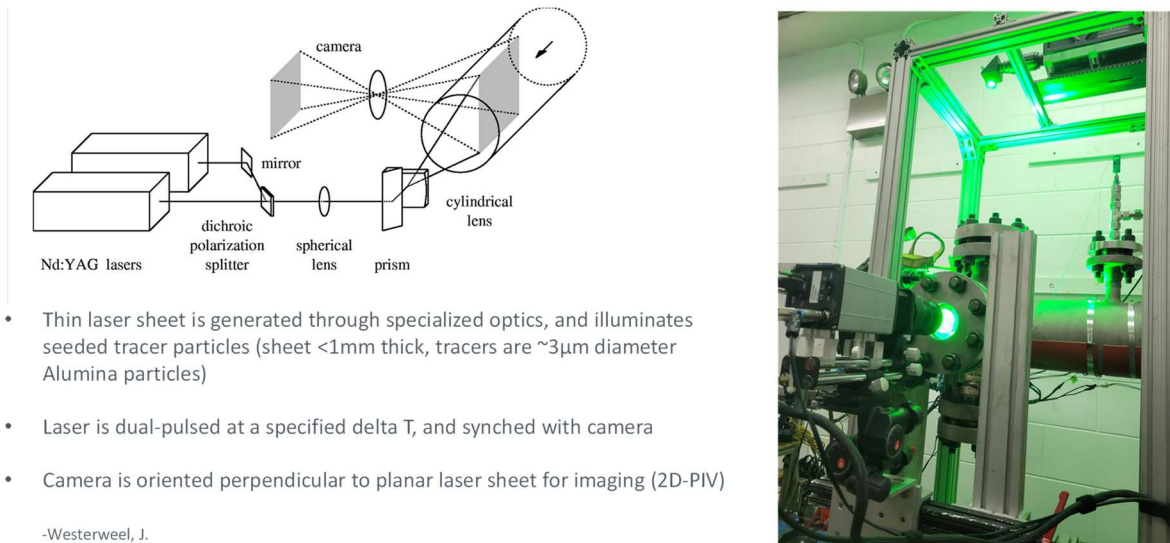

- Thin laser sheet is generated through specialized optics, and illuminates seeded tracer particles (sheet <1mm thick, tracers are ~3μm diameter Alumina particles)

- Laser is dual-pulsed at a specified delta T, and synched with camera

- Camera is oriented perpendicular to planar laser sheet for imaging (2D-PIV)

  -Westerweel, J.

Figure 18: Particle Image Velocimetry – Optical Configuration. Top Left [8]

While PIV is quite mature at this point, and is considered one of the most powerful fluid mechanics measurement techniques, in terms of available data output and fidelity; applications to high-pressure, supercritical fluids is extremely limited. While implementation of PIV at ambient pressure, and slightly elevated pressures can be relatively simple (Wind tunnels, water tunnels, free jets, supersonic wind tunnels, etc.), application to a sCO_2 flow field presents a multitude of challenges which have been outlined. Valori et al. recently presented the feasibility of PIV in a thermally conductive supercritical fluid (Trifluoromethane), with a critical point of 48 bar, and 26°C. The experimental setup was limited to a small 70 mm x 70 mm x 70 mm measurement domain where a Rayleigh–Bénard convection flow was studied. The apparatus and experiment showed the feasibility of PIV for these supercritical fluids, and highlighted some of the challenges, however, was limited to a fundamental, benchtop flow [13]. Lance, demonstrated the application of PIV to a small, closed vessel thermal convection flow using sCO_2 as the working fluid. This study again showed the feasibility of PIV as a measurement technique for sCO_2, but again, was limited to a small benchtop experimental demonstration [14]. PIV of a sCO_2 flow in a microchannel was also studied by Parahovnik et al.. While sCO_2 PIV was successfully demonstrated, the flow conditions and scale in microfluidic applications, differ substantially from a full-scale experiment, particularly with pressure containment needs [15]. ***To the author's knowledge, this work presents the first of its kind application of Particle Image Velocimetry to evaluate a problem of engineering interest at this size, and flow scale. This is also be the first application of PIV in a closed loop sCO_2 flow environment.***

Final Test Section Configuration and Calibration

The first test section configuration was fabricated from clear PVC plastic. While this material held structure and shape fairly well, optical clarity degraded over time similar to that of cast acrylic, albeit, at a much slower rate. Due to the length of tests and multiple cases to be run, a more robust material solution was chosen. The front and back main walls were refabricated out of aluminum, and new quartz sight windows were embedded into the plates. This setup allowed for a long-term structural solution with ideal optical qualities as all line-of-sight optics were converted to quartz. Figure 19 shows the previous test section assembly with the PIV calibration grid installed, and the final configuration aluminum walls. Note the calibration grid is installed in the vessel prior to any data acquisition and is imaged by the camera system in the final optical configuration (camera-to-laser relative locations, and optical light guide rods). This allows for the processing software to correct for any optical aberrations and ensure proper mapping when viewing through multiple optical mediums.
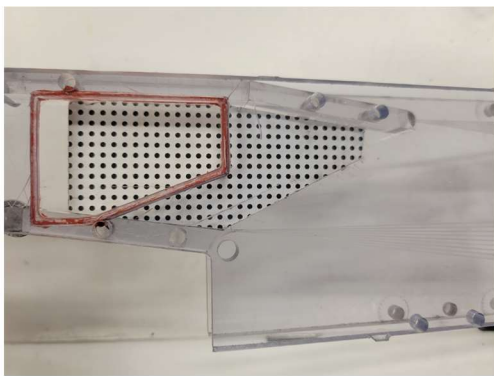
Previous Test Section with Quartz inset to PVC walls

Aluminum Walls

Figure 19: Calibration grid and final test section assembly

RESULTS AND DISCUSSION

Experimental Blade Performance Evaluation

Figure 20 shows zoomed images in the vicinity of both leading edges. With the high-resolution 5.5 Megapixel camera used and the current magnification level (46 pixels/mm), resultant particle image sizes are ~6 – 8 pixels, and maximum displacement shifts of ~5.5 pixels between laser pulses. With these characteristics, along with the higher overall seeding density, smaller interrogation windows can be used, which lead to higher final vector spatial resolution.
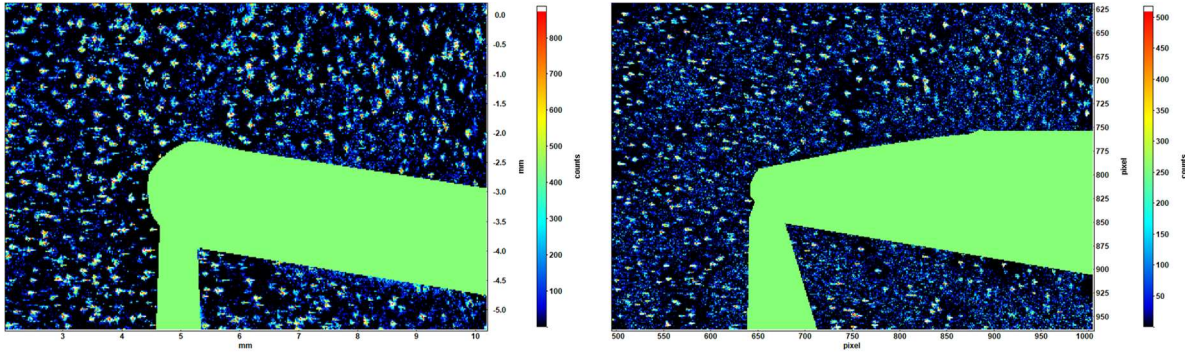
Figure 20: Final Testing Configuration PIV – Seeding Density Leading Edge

The PIV measurement domain is superimposed on the CAD view of the linear cascade as shown in Figure 21. The field of view captures 15 mm upstream of the lower blade's leading edge, and about 20 mm above, in the Y direction. The suction side of the lower blade is captured about 25 mm downstream. The measurement plane is on the blade span centerline. As the leading-edge flow field of the lower blade is of interest, this field of view is sufficient to characterize the performance of the Biased-Wedge.
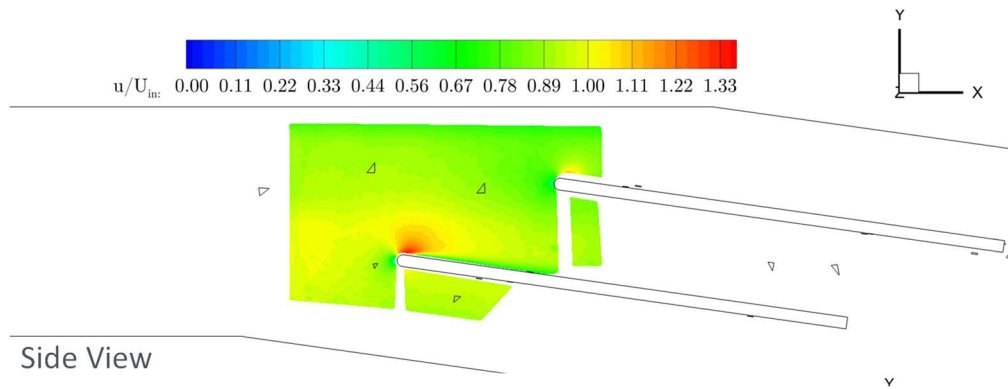

Figure 21: PIV Measurement Domain

With the improvements in seeding quality and particle image density, the final interrogation window size was able to be reduced to 16 x 16 pixels, and processed with a 75% window overlap. For robust cross-correlation a minimum number of particles must be present in the interrogation window, sparse seeding must use larger windows at the expense of final spatial resolution. With this configuration, the final effective vector spatial resolution achieved was ~ 0.08 mm x 0.08 mm. All of the results presented in this section are the mean velocity fields generated from an ensemble average of ~1,400 instantaneous vector fields.

Figure 22 shows the velocity magnitude superimposed with flow streamlines to better visualize the flow field. The right image shows the final vector resolution mesh which helps illustrate the excellent final spatial resolution of the processed velocity fields. The resultant vector spatial resolution for all results presented is ~0.08 mm x 0.08 mm. Based on the streamlines, the stagnation point occurs at the leading edge, and does not have a bias to the suction or pressure side. Note as previously discussed, the exit tailboards had to be adjusted by 1˚ to ensure a

centered leading-edge stagnation point. The stagnation point at the leading edge is clearly seen, and followed by an acceleration region on the suction side as flow travels around the leading edge.
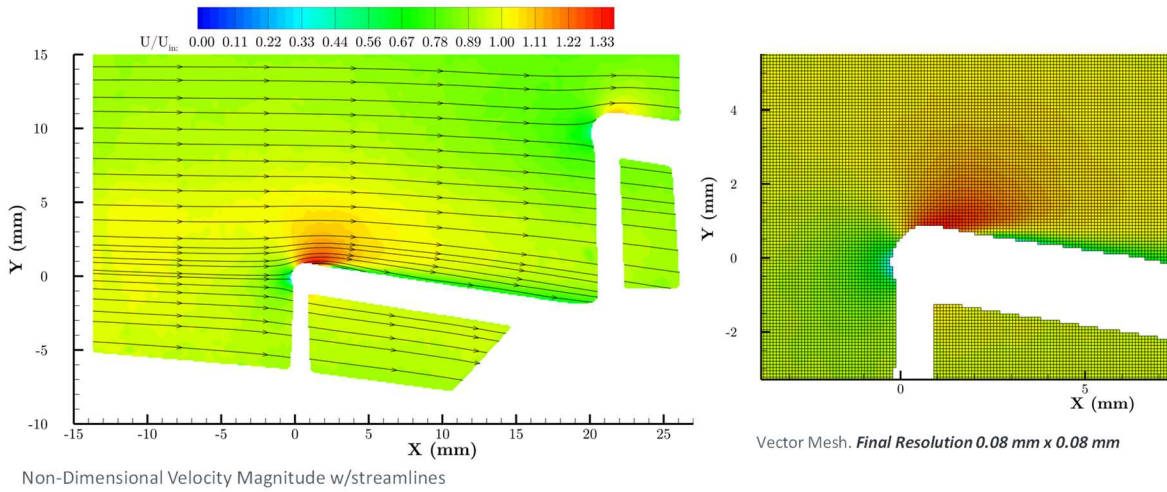

Non-Dimensional Velocity Magnitude w/streamlines

Vector Mesh. *Final Resolution 0.08 mm x 0.08 mm*

Figure 22: PIV Results – Baseline 90 Bar – Magnitude and Vector Resolution

Figure 23 shows the non-dimensional velocity components for the Biased-Wedge blade at 90 Bar. In contrast to the Baseline blade, the local flow acceleration at the leading edge has been delayed to the suction peak downstream at the location of maximum blade thickness. This gradual profile helps to reduce the suction side pressure gradient, as can be seen by the more gradual velocity increase and lower suction side velocity peak compared to the baseline blade.
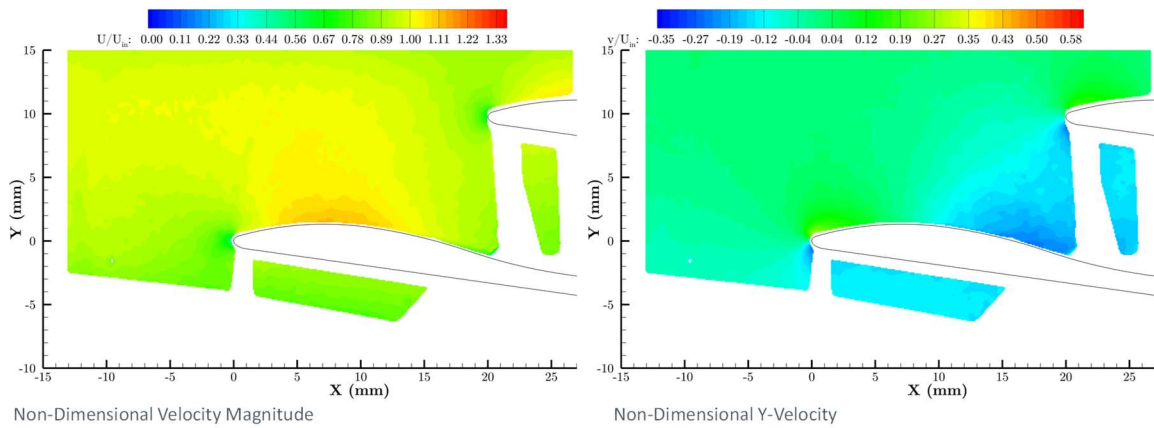

Non-Dimensional Velocity Magnitude

Non-Dimensional Y-Velocity

Figure 23: PIV Results – Biased Wedge 90 Bar – Velocity Components

A direct comparison of the Baseline and Biased-Wedge blades is shown in Figure 24 for the 90 Bar case. This figure highlights the leading edges and suction peak regions. In comparing the suction peak velocities, the Biased-Wedge blade shows a marked lower velocity in that region, along with a more spread-out suction peak region highlighting a lower pressure gradient. The baseline blade, at the suction peak, is marked by velocities ~20% higher than that of the Biased-Wedge.
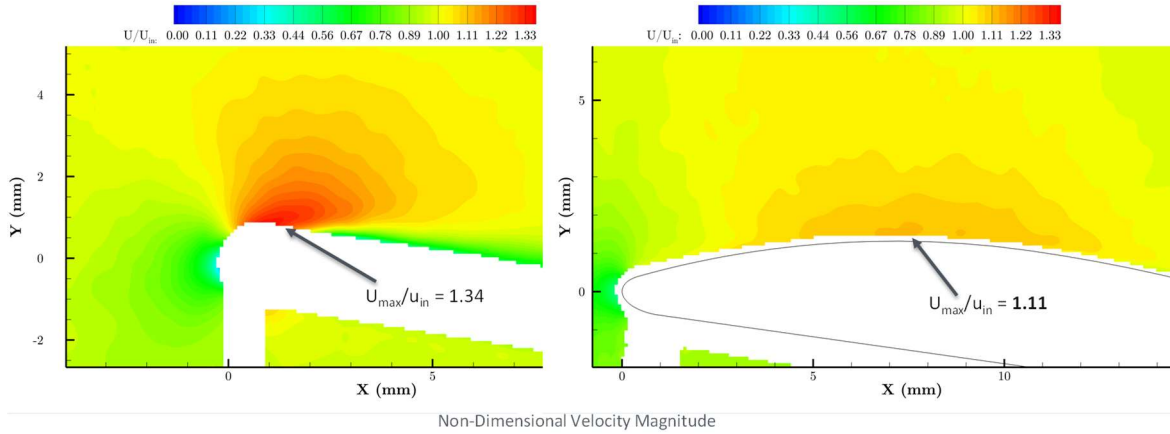
Figure 24: Blade Performance Comparison – 90 Bar – Zoomed on Leading Edges

CFD Validation with Experimental Data

After the final phase of experiments were concluded, experimental run conditions were provided to CRAFT to run companion numerical cases to further validate numerical results for this configuration. Boundary conditions are given in Table 1. Numerical simulation data were non-dimensionalized in the same manner as experimental data.

Blade	P (Bar)	Mass Flow Rate (kg/min)	T_upstream RTD (C)
Baseline	90.9	3.67	37.57
Biased Wedge	90.6	3.22	38.06
Baseline	80.7	2.56	37.67
Biased Wedge	80.0	2.46	37.89

Table 1. Thermodynamic Conditions for Tests at UCF

Figure 25 shows the velocity magnitude field for the Baseline blade experimental PIV case on the left, and CFD case on the right, for the 90 Bar condition. Here, a plane was extracted at the blade mid-span of the CFD results for comparison. The CFD shows good agreement with the experimental result. The flow's salient features and local suction peaks are captured well. The global velocity field, even upstream of the blade is also predicted. Suction velocity on Baseline was predicted within 5.2% of experiment.

Figure 26 shows the velocity magnitude field for the Biased-Wedge experimental PIV case on the left, and CFD case on the right, for the 90 Bar condition. Similar to the baseline, the CFD shows excellent agreement with the experimental result in capturing the overall flow field and main features. The peak suction velocity on the Biased-Wedge was predicted within 1%.
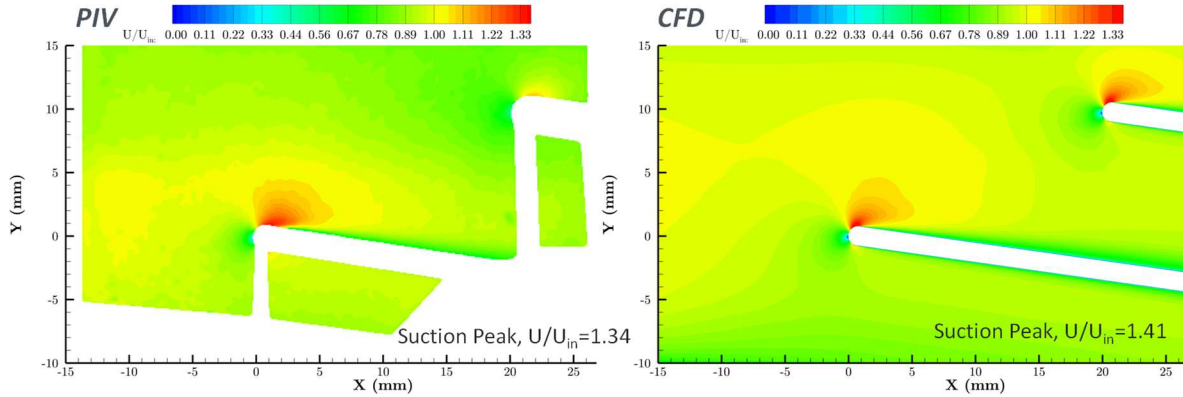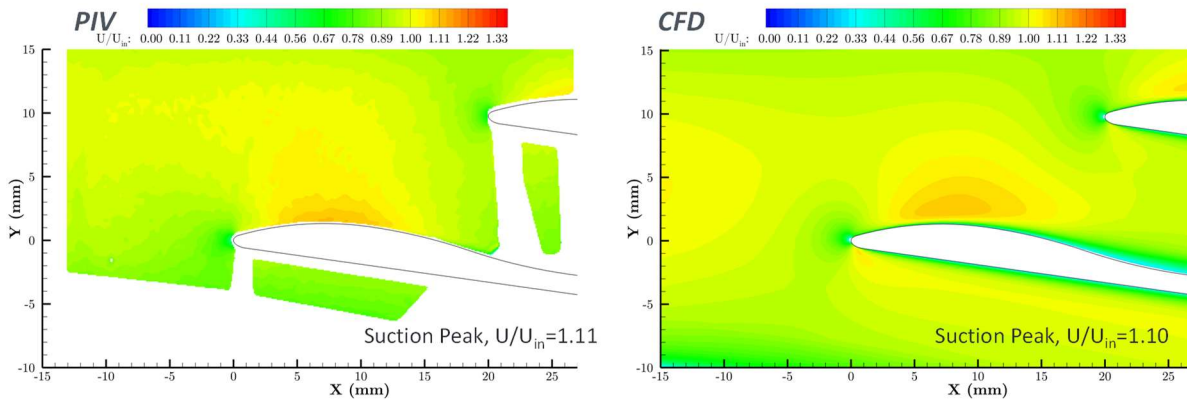
Figure 25: Comparison with CFD, 90 Bar – Baseline

Figure 26: Comparison with CFD, 90 Bar – Biased-Wedge

Simulations Near Critical Temperature (306K)

Simulations to evaluate the cascade over a range of higher velocities at reduced inlet temperatures and pressures that are closer to the critical point are presented here. These simulations will help identify when multi-phase effects begin in both design configurations. In the simulations reported in this section, the pressure was reduced to 8.0 MPa and the temperature was reduced to a nominal value of 306 K. The velocity values at the inlet ranged from 23 m/s to 43 m/s.

Details of the conditions for the various cases are shown in Table 2. The goal of these simulations is to identify the velocity range necessary to generate a large enough temperature drop on the suction surface to create subcritical conditions and initiate condensation. Multi-phase calculations were performed to quantify the extent of condensation and the concentration of liquid in the subcritical zone. As indicated in Table 2, the baseline blade experienced sub-critical temperatures starting at an inlet velocity of 33 m/s and condensation occurred at all higher velocities. In contrast, the biased wedge remained in the supercritical state for all the velocities here up to a value of 43 m/s which is a significant improvement. Additional increase in velocity to 46 m/s results in condensation being initiated on the biased wedge as well.

Analysis ID	Mass flow Rate (kg/s)	Inlet Velocity (m/s)	Inlet Temperature (K)	Inlet Pressure (MPa)	Baseline Configuration: Condensation	Biased Wedge Configuration: Condensation
1	8.14	42.9	306	8.22	Yes	No
2	7.27	38.8	306	8.14	Yes	No
3	6.12	33.1	306	8.08	Yes	No
4	5.25	28.5	306	8.05	No	No
5	4.37	23.9	306	8.03	No	No

Table 2. Parametric Study with Inlet Velocity for Baseline and Biased Wedge at Inlet Temperature of 306K

The temperature profile on the suction surface for the baseline and biased wedge foils are plotted for the two highest velocities of 38.8 m/s and 42.9 m/s in Figure 27. The temperature on the baseline configuration shows temperatures dropping to subcritical values as the flow accelerates with the temperature becoming lower as the velocity increases from 38.8 m/s to 42.9 m/s. The temperature contours at these two velocities are plotted in Figure 28 and Figure 29, respectively. The region of subcritical temperature (in blue) at the leading edge is very evident in the baseline configuration while in the biased wedge case the temperature drop is more muted and occurs further downstream near the maximum blade thickness.
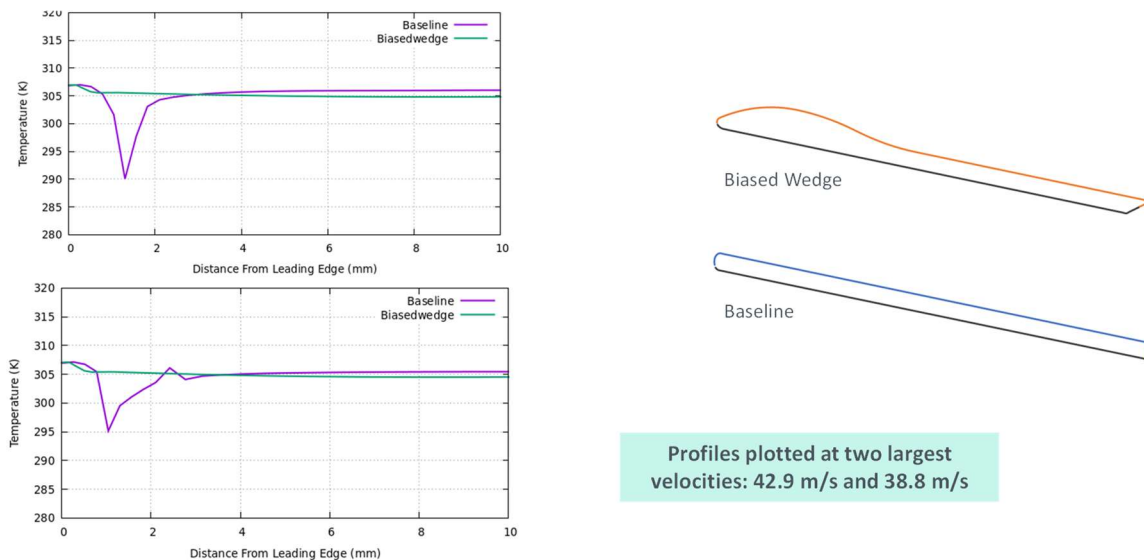

Figure 27: Temperature on Airfoil at Different Inlet Velocities: Green curve is the Biased Wedge while Purple curve is the Baseline blade

For the baseline configuration, the condensation at the leading edge for the two highest velocities, i.e., 38.8 and 42.9 m/s, are shown below in Figure 30, and Figure 31, respectively. We observe that condensation occurs in the region of the subcritical temperature which is consistent with the physics. As the velocity increased, the condensation region grows in dimension as the subcritical zone gets larger. Furthermore, the change in density due to condensation can modify the streamlines and affect the growth of the condensation zone.

Baseline
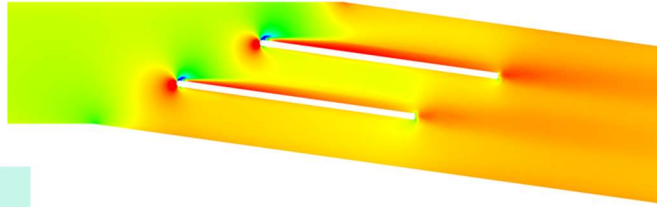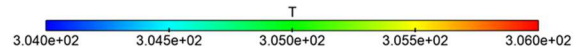
Biased Wedge

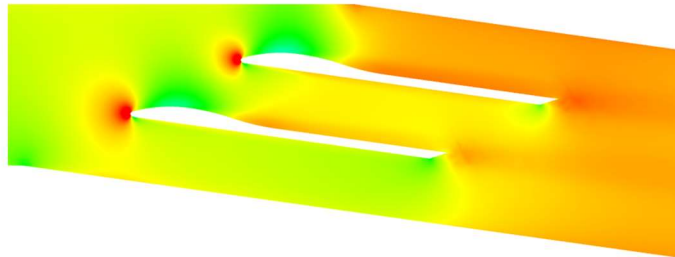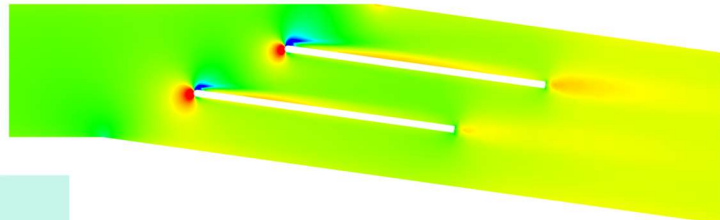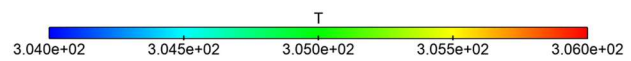*Figure 28: Temperature Contours 7.27 kg/s*

Baseline

Biased Wedge

Figure 29: Temperature Contours 8.14 kg/s

Baseline

Solution for 38.8 m/s

yliq2
0.000e+00   2.486e-01   4.972e-01   7.458e-01   9.944e-01

Leading-edge
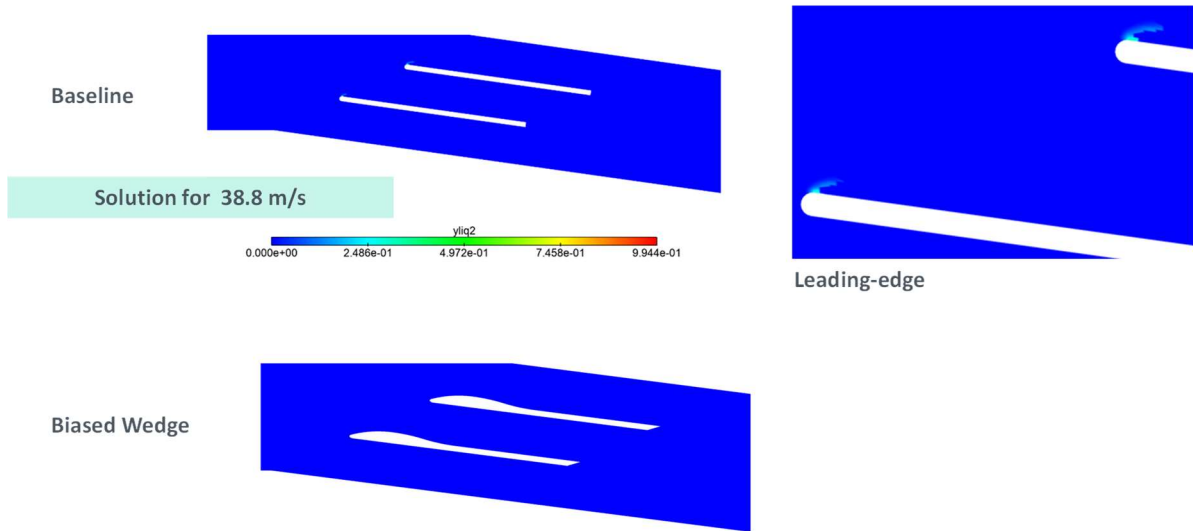
Biased Wedge

Figure 30: Liquid Condensate Concentration: 7.27 kg/s

Baseline

Solution for 42.9 m/s

yliq2
0.000e+00   2.486e-01   4.972e-01   7.458e-01   9.944e-01

Leading-edge

Biased Wedge

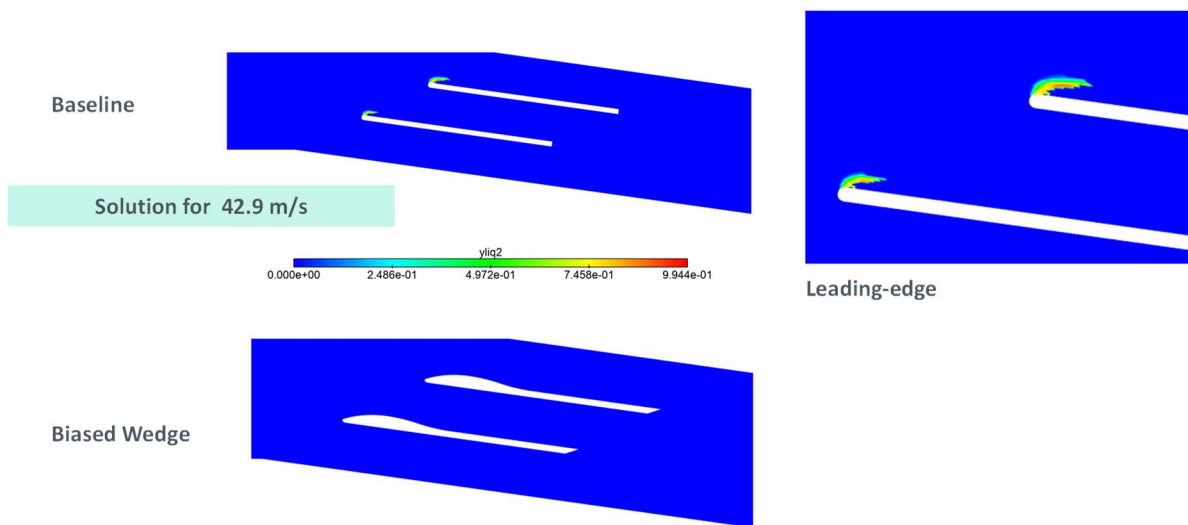*Figure 31: Liquid Condensate Concentration: 8.14 kg/s*

Biased-Wedge Performance for 5 Mwe Compressor Conditions in Sunshot Program

Simulations were also performed at a higher inlet temperature and pressure corresponding to the test conditions for the Hanwha compressor. We note under a previous effort, the CRUNCH CFD code had been validated for correctly predicting the mean performance of the Hanwha compressor at various inlet temperatures by comparing with test data obtained under the DoE Sunshot program [6]. In our effort here, we specify the inlet temperature corresponding to the design inlet temperature of the Hanwha compressor at 310 K. A parametric study was conducted for various inlet velocities as shown below in Table 3.

The results obtained indicate that the biased wedge remained effective till an inlet velocity of 92 m/s with no condensation observed as noted in Table 3. Increasing the velocity further to

98 m/s resulted in condensation on the suction surface. The temperature profile on the suction surface is shown below in Figure 32. It is observed that the minimum temperature remains supercritical for all velocities till 92 m/s. At 92 m/s the minimum temperature is 304 K. As the velocity increases further the temperature drops into the subcritical dome and phase change results.

INLET VELOCITY (m/s)	INLET TEMPERATURE (K)	INLET PRESSURE (MPa)	Phase Change
62	310	7.94	No
80	310	7.91	No
92	310	7.88	No
98	310	7.88	Yes

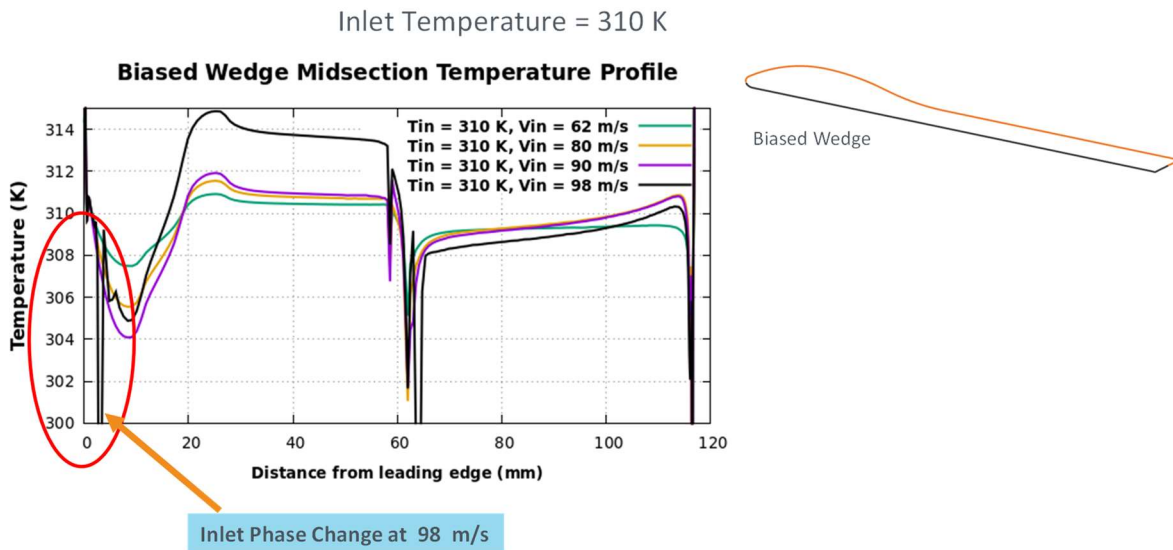*Table 3: Parametric Study for Biased Wedge Performance at 310 K*

Figure 32: Temperature Profiles on Biased Wedge for Different Inlet Velocities at Inlet Temperature of 310 K

The temperature contours at the various velocities are shown in Figure 33. It is observed that as the velocity increases, the temperature and pressure drop on the biased wedge become more pronounced. By 98 m/s the low temperature and low pressure is quite prominent as phase change and condensation sets in. It can also be seen that as the velocity increases, the flow contours show increasing non-periodicity between the two blade domains. These issues may need to be addressed for future testing at higher flow rates.
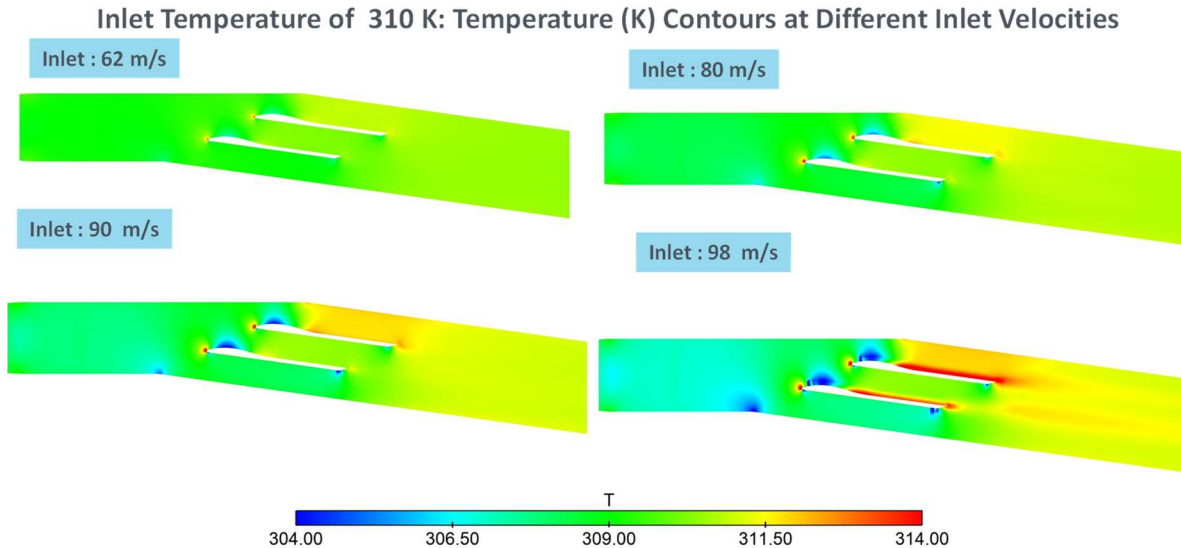
Inlet Temperature of 310 K: Temperature (K) Contours at Different Inlet Velocities

Inlet : 62 m/s

Inlet : 80 m/s

Inlet : 90 m/s

Inlet : 98 m/s

T

304.00   306.50   309.00   311.50   314.00

Figure 33: Temperature Contours for Biased Wedge at Various Inlet Velocities with Inlet Temperature of 310 K

CONCLUSION

In this study, a new design approach has been devised for the suction surface of compressor blades' leading edges. This methodology aims to significantly reduce pressure and temperature drops, potentially minimizing performance losses and damage resulting from phase change. Importantly, this innovative design, known as the "Biased-Wedge," introduces an expansion of the impeller blade's suction side, resembling more of an airfoil. The resulting blade camber aligns the leading edge more effectively with the incoming relative flow, avoiding the substantial incidence associated with conventional blades.

As part of this initiative, a cascade with two blades was designed. Subsequently, the cascade design was handed over to the UCF group for the conversion into a physical test apparatus. Integrated into a novel optical diagnostics pressure vessel, the test section allowed groundbreaking, first of their kind quantitative velocimetry measurements of sCO_2 compressor blade flow fields. Testing took place in the UCF sCO_2 loop at inlet pressures of 80 bar and 90 bar, with temperatures ranging approximately from 37.57 to 38.09°C. Due to pump limitations in the UCF test loop, the inlet velocity remained relatively low at around 0.8 m/s. Both simulations and test results at these conditions demonstrated that the Biased-Wedge design led to lower acceleration and smaller pressure drops on the suction surface, aligning with predictions.

Further numerical investigations of the Biased-Wedge were conducted at higher velocities to reflect conditions representative of the Sandia compressor (inlet temperatures of 306 K) and the higher energy Hanwha compressor (inlet temperatures of 310 K). The Biased-Wedge exhibited superior performance compared to the Baseline configuration. At an inlet temperature of 306 K, ranging velocities from 23 m/s to 43 m/s, the Baseline blade experienced sub-critical temperatures starting at 33 m/s, with condensation occurring at higher velocities. In contrast, the Biased-Wedge maintained a supercritical state for all velocities up to 43 m/s, marking a significant improvement.

For the simulations performed at a higher inlet temperature (310 K) corresponding to the

test conditions for the Hanwha compressor, the inlet velocity was varied from 62 to 98 m/s. Note that the Hanwha compressor inlet tip speed in the Sunshot test program was 83.43 m/s and this range encompasses the Hanwha inlet condition. The Biased-Wedge showed good performance and remained in the supercritical state till 92 m/s. This indicates that the Biased-Wedge holds potential for improving the performance of full-scale higher energy compressors.

REFERENCES

[1] L. Blanchette, "Investigation of Real Gas Effects on Centrifugal Compressor Analytical Methods for Supercritical CO_2 Power Cycles," Master's Thesis, Advisor - Jayanta Kapat, University of Central Florida, 2016.

[2] S.L. Dixon and C.A. Hall, Fluid Mechanics and Thermodynamics of Turbomachinery. Butterworth-Heinemann, Year: 2014.

[3]P. Cooper, D. Sloteman, E. Graf, and D. Vlaming, "Elimination of Cavitation-Related Instabilities and Damage in High-Energy Pump Impellers," in 8th International Pump Users Symposium, Texas A&M University, Houston, 1991, pp. 3–19.

[4] D. Sloteman and P. Cooper, "Design of High-Energy Pump Impellers to Avoid Cavitation Instabilities and Damage," in EPRI Power Plant Pump Symposium, Tampa, 1991.

[5] D. Sloteman, T. Wotring, P. March, D. McBee, and L. Moody, "Experimental Evaluation of High Energy Pump Improvements Including Effects of Upstream Piping," in 12th International Pump Users Symposium, Texas A&M University, Houston, 1995, pp. 97–110.

[6] Hosangadi, A., Weathers, T., Liu, Z., Pelton, R., Wygant, K., and Wilkes, J., "Numerical Predictions of Mean Performance and Dynamic Behavior of a 10 Mwe SCO_2 Compressor with Test Data Validation," J. Eng. Gas Turbines Power. Dec 2022, 144: 1210.

[7]. Venkateswaran, S., and Merkle, C.L., "Analysis of Preconditioning Methods for the Euler and Navier-Stokes Equation", VKI Lecture Series Monographs on Computational Fluid Dynamics, VI LS 1999-03, von Karman Institute, March 1999.

[8]. Hosangadi, A., Sachdev, J., and Venkateswaran, S., "Improved Flux Formulations for Unsteady Low Mach Number Flows", Seventh International Conference on Computational Fluid Dynamics, Paper No. ICCFD7-2202, Big Island, Hawaii, July 2012

[9]. NIST: Thermophysical Properties of Fluid Systems. Online Access at https://webbook.nist.gov/chemistry/fluid/

[10]. Hosangadi, A., Liu, Z., Weathers, T., Ahuja, V., Busby, J., "Modeling Multiphase Effects in CO_2 Compressors at Subcritical Inlet Conditions", J. Eng. Gas Turbines Power, Aug 2019, 141: 081005-1.

[11]. Brinckman, KW, Hosangadi, A, Liu, Z, and Weathers, T. "Numerical Simulation of Non-Equilibrium Condensation in Supercritical CO_2 Compressors." Proceedings of the ASME Turbo Expo 2019: Turbomachinery Technical Conference and Exposition, Phoenix, Arizona, USA. June 17–21, 2019.

[12] Adrian, R.J., Westerweel, J., 2011, "Particle Image Velocimetry," Cambridge University Press, New York, NY., USA.

[13] Valori, V., Elsinga, G.E., Rohde, M., Westerweel, J., van der Hagen, T.H.J.J., "Particle Image Velocimetry Measurements of a Thermally Convective Supercritical Fluid," Experiments in Fluids, Vol. 60, 143, 2019.

[14] Lance, B.W., "Flow Distribution Measurements in sCO_2," 6th International Supercritical CO_2 Power Cycles Symposium, SAND2018-2311C, 2018.

[15] Parahovnik, A., Park, S., Peles, Y., Vasu, S., " First Demonstration of PIV Measurements in sCO_2 Flows Inside Microchannel Near The Critical Point, "7th International Supercritical CO_2 Power Cycles Symposium, 2020.

ACKNOWLEDGEMENTS

Disclaimer: "This report was prepared as an account of work sponsored by an agency of the United States Government. Neither the United States Government nor any agency thereof, nor any of their employees, makes any warranty, express or implied, or assumes any legal liability or responsibility for the accuracy, completeness, or usefulness of any information, apparatus product, or process disclosed, or represents that its use would not infringe privately owned rights. Reference herein to any specific commercial product, process or service by trade name, trademark, manufacturer, or otherwise does not necessarily constitute or imply its endorsement, recommendation, or favoring by the United States Government or any agency thereof. The views of and opinions of authors expressed herein do not necessarily state or reflect those of the United States Government or any agency thereof."